ELSEVIER

Relations of crystal structure to magnetic properties in the quasi-one-dimensional compound $PbNi_{1.88}Mg_{0.12}V_2O_8$

I. Mastoraki,[a] A. Lappas,[a,*] J. Giapintzakis,[a,b] D. Többens,[c] and J. Hernández-Velasco[c]

[a] Institute of Electronic Structure and Laser, Foundation for Research and Technology-Hellas, P.O. Box 1527, 711 10 Heraklion, Greece
[b] Department of Materials Science and Technology, University of Crete, P.O. Box 2208, 710 03 Heraklion, Greece
[c] Berlin Neutron Scattering Center, Hahn-Meitner-Institut, Glienicker Strasse 100, D-14109 Berlin, Germany

Abstract

The crystal structure of the quasi-one-dimensional oxide $PbNi_{1.88}Mg_{0.12}V_2O_8$ has been studied by Rietveld analysis of combined high-resolution neutron and X-ray powder diffraction data at 300 K and at low temperatures. The $(Ni/Mg)O_6$ octahedral units share a common edge and form spiral chains along the c-axis of the tetragonal unit cell, without deviating the $I4_1cd$ ($Z = 8$) symmetry upon cooling. DC magnetic susceptibility measurements show that the system undergoes a magnetic phase transition below $T_N \cong 3.4$ K. Rietveld analysis of the medium resolution neutron powder diffraction data confirms that impurity-induced antiferromagnetic order (with propagation vector, $\kappa = [000]$) takes over from the Haldane ground state of the parent compound. The power-law [$\beta = 0.31(3)$] temperature evolution of the strongest magnetic Bragg peak intensity indicates three-dimensional Ising-type magnetic interactions, while the reduced magnitude of the Ni^{2+} moment [$\langle \mu \rangle = 0.98(3) \mu_B$] suggests important zero-point spin fluctuations. Structural considerations are consistent with small changes in the interatomic distances around the bridging tetrahedral VO_4 entities separating the chains. However, no bulk structural phase transition concurrent to the Néel ordering is found. We show that the modification of intra- and inter-chain Ni–Ni distances upon cooling promotes the magnetic coupling of the end-of-chain liberated $S = 1/2$ spins and leads to antiferromagnetic ordering.
© 2004 Elsevier Inc. All rights reserved.

1. Introduction

A great deal of attention is currently being focused on low-dimensional quantum magnets, which are simple models of magnetism, and demonstrate a broad spectrum of complex quantum-mechanical phenomena. In these systems quantum fluctuations destroy long-range magnetic order (LRO) at any temperature. As such, one-dimensional (1D) quantum antiferromagnets (AF) are particularly interesting and worthy examining the influence of the significant zero-point quantum fluctuations on their magnetic properties. Some intriguing phenomena recently observed in low-dimensional systems include the spin-Peierls (SP) transition in $S = 1/2$ Heisenberg chains with strong spin-lattice interac-

tions [1], the appearance of the Haldane gap in integer spin Heisenberg chains [2] and the high-temperature superconductivity occurring in layered cuprates consisting of two-dimensional (2D) CuO_2 planes [3]. Subsequently, several detailed studies have been performed on the doping effects of such ground states and the phenomenon of the impurity-induced phase transition to long-range antiferromagnetic ordering (LRAFO) has been verified. Among these is worth noting the first purely inorganic SP compound, namely $CuGeO_3$ [4]. Indeed, various experiments confirmed that substitution of Cu^{2+} ions by either non-magnetic (e.g., $S = 0$: Mg^{2+}, Zn^{2+} [5,6]) or magnetic chemical impurities (e.g., $S = 1$ Ni^{2+} or $S = 5/2$ Mn^{2+} [6]) causes transitions to LRAFO independently of the S value of the impurity.

The search for chemical analogues led to a new low-dimensional $S = 1$ spin system, the $PbNi_2V_2O_8$ compound, which exhibits a Haldane-type gap in its

*Corresponding author. Fax: +30-2810-391305.
E-mail address: lappas@iesl.forth.gr (A. Lappas).

magnetic excitation spectrum [7,8]. The $PbNi_2V_2O_8$ compound is isostructural to the alkaline rare-earth vanadate $SrNi_2V_2O_8$ [9]. The distinguishing structural feature is the presence of the screw chains, which consist of edge-shared NiO_6 octahedra that run along the c-axis. The chains are separated by non-magnetic VO_4 tetrahedra and Pb^{2+} ions. Such a structure results in a quasi-one-dimensional arrangement of the Ni^{2+} ($S = 1$) spins where intra-chain nearest-neighbor Ni–Ni interactions are dominant. The quasi-one-dimensionality of the structure appears to be instrumental in determining the bulk physical properties and especially that of the magnetic behavior.

Furthermore, the problem of the impurity-induced AF order for this new system has been recently put under investigation to explore possible similarities to the doping effects observed in the SP compound $CuGeO_3$. In $PbNi_2V_2O_8$, the spin vacancy induced LRAFO has been recently confirmed by magnetic susceptibility [7], neutron powder diffraction and muon spin relaxation (μ^+SR) measurements [10]. This material is the first example of an inorganic Haldane chain compound that orders antiferromagnetically by doping with non-magnetic ($S = 0$) ions. It appears that the role of the inter-chain interactions is crucial in this system.

Shender and Kivelson [11] were the first who qualitatively discussed the possibility of spin vacancy-induced long-range order (LRO) in a Haldane-gap system. Experimental realization of this theoretical suggestion involved the substitution of nonmagnetic Mg^{2+} ions for Ni^{2+} ions [7]. The temperature dependence of the magnetic susceptibility for a series of $PbNi_{2-x}Mg_xV_2O_8$ powder samples ($x = 0 - 0.24$), showed that the characteristic thermally activated gap behavior observed in the undoped compound is gradually suppressed and a pronounced peak is observed in the low temperature susceptibility, with a maximum of ~ 3.5 K at a composition $x \cong 0.16$ [12]. In addition, an enhancement of the magnetic susceptibility is observed, which scales with Mg concentration, x. This behavior has been attributed to the presence of free $S = 1/2$ spins at the ends of the Ni chains severed by the spin vacancies [13].

The appearance of $S = 1/2$ 'edge spins' around both sides of the spin vacancies has been rigorously explained by the valence bond solid (VBS) model [14]. Experimentally Smirnov et al. [15] confirmed this phenomenon, by measuring the electron spin resonance (ESR) above the Néel point for a series of powder samples with $0 \leqslant x \leqslant 0.12$. Moreover, Zorko et al. [16] argued that the frequency dependence of the ESR signal observed at low temperatures, in samples with $0 \leqslant x \leqslant 0.24$, indicates a magnetic coupling between the chain-end spins on both sides of the Mg^{2+} impurity. This picture explains well the enhancement of the inter-chain coupling through the interaction of the free moments with the Ni^{2+} spins on

the neighboring chains and finally the establishment of a LRO state at low temperatures [17].

The purpose of this study is to present a detailed structural analysis of a selected member of the series $PbNi_{2-x}Mg_xV_2O_8$ with $x = 0.12$. We show that this compound undergoes a transition from a paramagnetic state to a 3D LRO AF state below ~ 3.4 K. Structural considerations enabled us to obtain useful insight on the superexchange pathways that govern the magnetic properties. Our data indicate that the magnetic phase transition is not accompanied by a bulk structural phase transformation. However, small changes in the bond lengths occur upon cooling. We discuss how this effect may alter the local geometry and influence the magnetic exchange interactions.

2. Experimental

Polycrystalline powders of the $PbNi_{1.88}Mg_{0.12}V_2O_8$ compound (5 g) were synthesized via the citrate sol–gel method using stoichiometric quantities of the following high-purity (99.9%) reagents: V_2O_5, $Ni(NO_3)_2 \cdot 6H_2O$, $Pb(NO_3)_2$, $Mg(NO_3)_2 \cdot 6H_2O$. After the V_2O_5 was completely dissolved in a solution of 100 mL distilled water with 10 mL HNO_3 under stirring and low heating ($\sim 60°C$), hydrolysis and condensation was promoted by adding 1 mL ethylene glycol for each gram of expected final product, the stoichiometric amount of solid citric acid ($C_6H_8O_7$) and the remaining starting materials. Gelation took place at $\sim 100°C$. The resulting gel was dried at 150°C overnight, and then it was heated at 480°C for 16 h to eliminate carbon-containing species. Following the completion of this process, the powder was pressed into a pellet, which was heated at 700°C for a total of 12 days. Every 3 days the sintering procedure was interrupted and the sample was ground. The high-temperature reactions were carried out in an alumina combustion boat. Phase purity of the final compound was checked by X-ray powder diffraction using a Rigaku D/MAX-2000H rotating anode diffractometer with Cu$K\alpha$ radiation and a secondary pyrolytic graphite monochromator. For quantitative analysis, X-ray diffraction (XRD) data were collected at room temperature (300 K) in the interval $10° \leqslant 2\theta \leqslant 130°$ with a step of $0.02°$ and a counting time of 29 s per step. All the peaks were indexed on the basis of the tetragonal space group $I4_1cd$ except for two peaks at $2\theta \cong 17.78°$ and $27.84°$, which have been attributed to a small amount of an unknown additional phase. A Guinier camera at the BENSC facility, with Cu$K\alpha_1$ radiation ($\lambda = 1.54056$ Å) and Si ($a = 5.430881$ Å) as internal standard, was used for the low-temperature study of our samples. High-statistics data were collected at 12 K in transmission geometry, with 2θ steps of $0.02°/50$ s and within the range of diffraction angle $6° \leqslant 2\theta \leqslant 100°$.

Neutron diffraction data were collected on the high-resolution E9 and the medium-resolution E2 and E6 powder diffractometers of the research reactor BER II in Berlin (BENSC/HMI), using wavelengths 1.798, 2.398 and 2.444 Å, respectively. About 4.5 g of the sample contained in a cylindrical vanadium can ($\varnothing = 8$ mm), were used in each case. The high-resolution data were obtained both at high (300 K/8 h) and low (12 K/8 h, 2 K data sets of 8 and 7 h each) temperatures, over a wide range of $5° \leqslant 2\theta \leqslant 155°$ (step width $\Delta 2\theta = 0.078°$). The medium-resolution data (12 h each) were collected over the range $5° \leqslant 2\theta \leqslant 85°$ (step width $\Delta 2\theta = 0.2°$) at temperatures below (1.58 K) and above (6 K) the transition temperature identified by the peak in the χ vs. T experiment. In order to investigate the temperature evolution of the magnetic phase, additional neutron profiles of limited 2θ-range ($28–48°$, step width $\Delta 2\theta = 0.1°$) and shorter time-duration (~ 80 min each) were collected between $1.6 < T \leqslant 3.6$ K, in 11 steps of $\Delta T \sim 0.17$ K, using a standard He cryostat. All the powder diffraction data were analyzed with the Rietveld method by employing the program FULL-PROF [18].

The bulk magnetic behavior of the polycrystalline compound was examined by DC magnetic susceptibility measurements, between 1.8 and 300 K, in an applied magnetic field of 0.1 T using an Oxford Instruments MagLab EXA extraction magnetometer.

3. Results and discussion

3.1. Magnetic susceptibility measurements

The temperature dependence of the DC magnetic susceptibility, χ, for PbNi$_{1.88}$Mg$_{0.12}$V$_2$O$_8$ is shown in Fig. 1. The measurements were made upon warming both after zero-field cooling (ZFC) and field cooling (FC) of the sample. In both cases, a prominent peak appears at $T_N \cong 3.39$ K, which is a signature of a magnetic phase transition. The magnitude of the susceptibility presented in Fig. 1 is in a good agreement with that of Ref. [7]. The small thermomagnetic irreversibility observed below T_N, between the ZFC and FC curves, has also been observed in other members of the series and has been discussed in terms of metamagnetic behavior in Ref. [10]. The magnetic susceptibility obeys the Curie–Weiss law, $\chi = C/(T - \theta)$, in the temperature range 150–300 K (inset of Fig. 1). From the Curie–Weiss fit, we estimate the effective magnetic moment per Ni^{2+} ion, $\mu_{eff} = 3.302(1)\,\mu_B$ ($2.98\,\mu_B$, $x = 0.24$) and the paramagnetic Curie temperature, $\theta = -426(1)$ K (-313 K, $x = 0.24$). The large negative value of θ indicates the existence of strong antiferromagnetic exchange interactions for the Ni atoms in the chains. The experimentally determined
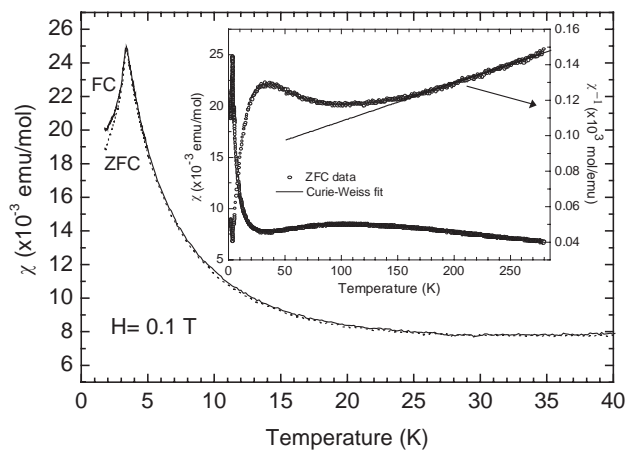

Fig. 1. Temperature dependence of the ZFC and FC molar magnetic susceptibility $\chi(T)$ for PbNi$_{1.88}$Mg$_{0.12}$V$_2$O$_8$ in a magnetic field $H = 0.1$ T. *Inset*: The temperature dependence of the reciprocal susceptibility χ^{-1} between 1.8 and 300 K. The fit ($150 < T < 300$ K) to the Curie-Weiss behavior is shown.

value of the effective moment is almost but not quite close to the calculated spin-only value of 2.83 μ_B, for the Ni^{2+} ion. If the spin-orbit coupling ($L = 3$) is included to calculate the magnetic moment for a free ion, as $\mu_{eff} = [L(L+1) + 4S(S+1)]^{1/2}\,\mu_B$, we obtain $\mu_{eff} = 4.47\,\mu_B$. To this extent, the relatively large observed moment can be justified if the orbital angular momentum of the Ni ion is only partially quenched. The inferred non-zero orbital contributions are in line with early ESR work suggesting an enhanced Landé factor, $g \sim 2.2$, for the PbNi$_{2-x}$Mg$_x$V$_2$O$_8$ series ($x \leqslant 0.24$) [16].

3.2. Magnetic neutron diffraction

In order to elucidate the nature of the magnetically ordered ground state in PbNi$_{1.88}$Mg$_{0.12}$V$_2$O$_8$, we performed medium-resolution neutron powder diffraction studies. We isolated the magnetic Bragg peaks using the subtraction technique, i.e., the nuclear-diffraction pattern (at 6 K) above the ordering temperature is subtracted from the pattern (at 1.58 K) obtained at temperatures below the transition temperature. This technique can be used when there is no significant structural distortion and the temperature variation of the lattice parameters is not considerable compared to the instrumental resolution. The resulting magnetic (1.58–6 K) difference plot (Fig. 2) was analyzed with the Rietveld method by employing a single-phase model accounting for the orientation of the spins and the magnitude of the moment per ion. Some details regarding this procedure have been reported elsewhere with respect to the analysis of neutron data for other members of the Mg- ($x \cong 0.24$) [10] or Co-($x \cong 0.08$) [19] substituted PbNi$_2$V$_2$O$_8$ series. In brief, all the magnetic peaks were indexed in the $P1$ space group for a given set of tetragonal lattice constants of the nuclear cell,
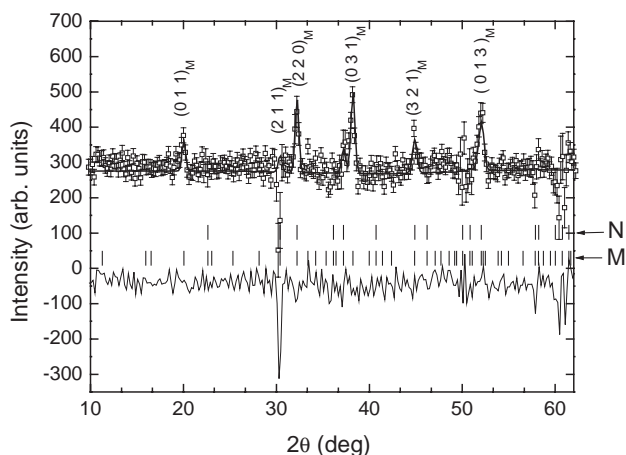
Fig. 2. Rietveld fit (solid line) of the neutron magnetic diffraction pattern (open circles) for $PbNi_{1.88}Mg_{0.12}V_2O_8$, obtained by subtraction of the 1.58 K profile from that at 6 K. The difference curve is shown at the bottom of the plot. Magnetic reflections (M) are indexed on the basis of a propagation vector $\kappa = [000]$. N stands for the nuclear reflections (space group: $I4_1cd$).

meaning that the magnetic unit cell coincides with the chemical one and a magnetic propagation vector $\kappa = [000]$ defines the mode of ordering. The orientation of the ordered moments was determined by finding the best agreement between the integrated intensities of the magnetic Bragg peaks in the experimental difference profile (1.58–6 K) and the patterns calculated for different spin configurations. Since the compound under consideration crystallizes in a uniaxial system, powder neutron diffraction cannot lead to unambiguous determination of the magnetic moment direction [20], only the angle between the spin direction and the unique (c) axis can be determined. Accordingly, our data would only distinguish if the spin lies in a direction parallel or perpendicular to the unique axis. We note that the 16 Ni atoms of the $PbNi_{2-x}Mg_xV_2O_8$ nuclear unit cell, in the $I4_1cd$ space group, adopt a 4×4 arrangement along a four-fold screw axis. Then, our exploratory analysis examined the *coupling* of all the symmetric ferromagnetic (F) or antiferromagnetic spin spirals, i.e.

$$\begin{bmatrix} + & + \\ + & + \end{bmatrix}, \begin{bmatrix} + & - \\ + & - \end{bmatrix}, \begin{bmatrix} + & - \\ - & + \end{bmatrix},$$

that were possible to be formed. This represents helical Ni-chain motifs (projected in the *ab* plane) propagating along the *c*-axis with $+$ or $-$ indicating spin 'up' or 'down' orientation with respect to the unique axis. Their *coupling* in the unit cell, in all possible combinations, results in 6 ($= 3 \times 2$) variants or refinable magnetic ordering models. The agreement (R-)factors from the profile refinement were monitored in an effort to verify the suitability of the model. Very poor results, without convergence, conferred with a helical structure where the moments were in the *ab*-plane and rotated by 90° from Ni to Ni site along the *c*-axis. More importantly,

the absence of characteristic (hkl) classes of reflections in the experimental difference profile, limits the number of probable models. For instance, simple F-chains antiferromagnetically coupled to each other is expected to produce strong Bragg scattering at the (100)/(010) or (110) positions, which however did not appear, making it an unlikely model. This procedure let us conclude that, although of a different doping level, $PbNi_{1.88}Mg_{0.12}V_2O_8$ adopts the same magnetic structure as the $x \cong 0.24$ composition. The Ni moments couple antiferromagnetically (AF) both along the *c*-direction and within the *ab*-plane. This spin-configuration results in a Rietveld fit of reasonable quality ($R_{wp} = 8.64\%$, $R_{exp} = 7.69\%$, $\chi^2 = 1.26$) (Fig. 2).

The AF arrangement of the Ni-spin chains is depicted as an inset in Fig. 3. The average magnetic moment per Ni ion in the AF spin configuration is $\langle \mu \rangle = 0.98(3)\,\mu_B$. This is marginally different from the $0.9(1)\,\mu_B/Ni^{2+}$ in the $PbNi_{1.76}Mg_{0.24}V_2O_8$ compound, which is located in the heavily doped region of the x vs. T_N phase diagram [12]. In the latter, the T_N against Mg-composition presents a broad maximum at $x \sim 0.16$. However, our neutron data prevent us at this stage from verifying if the staggered moment, $\langle \mu \rangle / Ni$, versus x follows also a similar behavior. It is worth noting though the deviation of $\langle \mu \rangle$ from the theoretical spin-only value ($\mu = gS = 2\,\mu_B$) for $S = 1$ Ni^{2+} in LRO state. Ni–O covalency effects in addition to quantum-mechanical 'zero-point' spin fluctuations can be responsible for this. Reduced experimental values of $\langle \mu \rangle$ for the easy-axis spin-1 antiferromagnetic Heisenberg chain system $CsNiCl_3$ [21], has been shown before to reflect the dimensionality of the magnetic correlations. It is a common feature in prototypical 1D-AF Haldane systems, such as R_2BaNiO_5 (R = rare earth), that the Ni^{2+} saturation moment in the 3D magnetically ordered phase to be somewhat reduced from $2\,\mu_B$ [22–24].
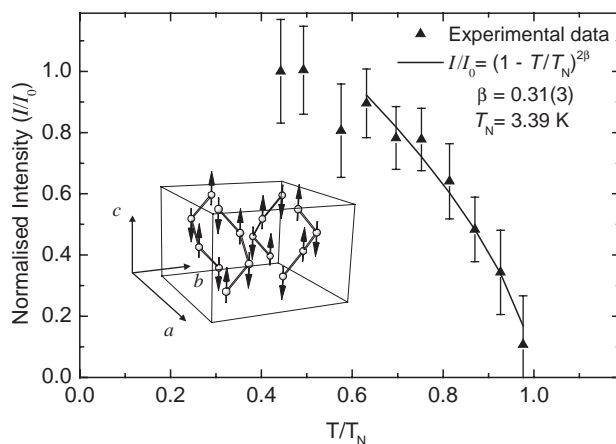

Fig. 3. Temperature evolution of the strong (031) magnetic Bragg peak intensity in the temperature range 1.6–3.6 K. *Inset:* One chemical unit cell with the Rietveld refined spin configuration ($\kappa = [000]$) of the Ni^{2+} ions in $PbNi_{1.88}Mg_{0.12}V_2O_8$.

Fig. 3 displays the temperature evolution of the normalized integrated intensity of the strongest magnetic Bragg peak (031). It was obtained by fitting a Gaussian function to the respective peak at each temperature. In general, the ordered-moment size is $\langle\mu\rangle \propto (I_{031})^{1/2}$. The data for temperatures between 2.1 and 3.3 K have been fitted to a power-law expression of the type $I \sim I_0[1-(T/T_N)]^{2\beta}$. T_N has been kept fixed at the value obtained from the position of the peak in the DC magnetic susceptibility measurements, namely $T_N = 3.39$ K. The least-squares result for the critical exponent, $\beta = 0.31(3)$, is close to the one predicted by the three-dimensional *Ising* model, $\beta_{Ising} = 0.326$ [25]. This observation suggests the existence of easy-axis anisotropy in the antiferromagnetic interactions as the spins are aligned either parallel or antiparallel to the *c*-axis. The *Ising*-like character of the spin alignment in this compound, is in agreement with the large negative value ($D<0$=easy-axis) of the single-ion anisotropy constant, $D = -0.45$ meV, derived from the analysis of the inelastic neutron scattering spectra of the isostructural (vide infra) parent compound $PbNi_2V_2O_8$ [17].

3.3. Structural refinement

Structural refinements on $PbNi_{1.88}Mg_{0.12}V_2O_8$ were carried out by Rietveld analysis of *combined* X-ray (XRD) and neutron powder diffraction (NPD) data at 300 K and low temperatures (12 K). This procedure offers the advantage to determine simultaneously the position of the vanadium atoms, which have small coherent scattering length for neutrons and the light oxygen atoms, which display relatively small atomic scattering factors for X-rays.

Fig. 4 illustrates the combined Rietveld analysis of the NPD and XRD data taken at 300 K, with a very good agreement between the observed and calculated patterns. For all refinements of the crystal structure, we used as starting parameters those obtained from single-crystal X-ray diffraction data of the $SrNi_2V_2O_8$ compound [9]. A pseudo-Voigt profile function convoluted with axial divergence was employed to generate the line shape of the diffraction peaks for the NPD and (Guinier geometry) XRD patterns. In addition, a Thompson-Cox-Hasting pseudo-Voigt profile function was chosen to generate the line shape of the diffraction peaks for the XRD pattern in the Bragg-Brentano geometry. The NPD background was fitted by a polynomial function, while that associated with the XRDs was linearly interpolated through selected points. The refinements allowed us to describe with good confidence the crystal structure, namely the atomic positions, the occupation factors and the lattice parameters. In addition, this gave a good description of the thermal motion for all the atoms, somehow different from that in the isostructural $SrNi_2V_2O_8$ compound. Data collection conditions and

refinement details[1] at 2, 12 and 300 K are summarized in Table 1 while structural parameters are listed in Table 2a–c. The atomic site occupancies, η, for the Ni and Mg were also refined within the accuracy of the present work. For example, they were found to be $\eta_{Ni} = 1.86(2)$ and $\eta_{Mg} = 0.14(2)$ at 300 K, showing only marginal deviation from the nominal values.

The overall crystal structure determined herewith is essentially the same to that reported before [10], however, new insight has been gained due to the higher resolution of the current neutron experiments and the additional statistical accuracy offered by the *combined* Rietveld analysis. The quasi-one-dimensional character of the $PbNi_{1.88}Mg_{0.12}V_2O_8$ structure arises from the spiral-chain arrangement of the distorted, edge-shared $(Ni/Mg)O_6$ octahedra along the *c*-direction and their separation by non-magnetic V^{5+} and Pb^{2+} cations. Selected bond distances and angles are given in Tables 3 and 4, for all the temperatures studied. The mean Ni–O distance falls in the range of the average Ni–O bonds observed in other compounds consisting of NiO_6 octahedral units, such as the rhombohedral $LaNiO_3$ (i.e. 1.935 Å) [26] and the orthorhombic La_2NiO_4 (i.e. 2.105 Å) [27] perovskites. For ease in the discussion below, we define the 2 K Ni–O(2), Ni–O(3) short bonds together with the Ni–O(1), Ni–O(4) ones as equatorial (E) distances, while the longer Ni–O(2), Ni–O(3) we assume to indicate the apical (A) oxygen connectivity in the *c*-direction (Fig. 5). We suggest that the observed elongation of the NiO_6 octahedra along the *c*-axis may be due to the ligand field effect around Ni^{2+} ion, which lifts the degeneracy of the five d^8 orbitals giving rise approximately to three degenerate t_{2g} orbitals that are lower in energy than the other two of e_g symmetry. The e_g state consists of two single occupied orbitals, one along the apical axis of the octahedron (d_{z^2}) and the other perpendicular to *c*-axis ($d_{x^2-y^2}$). In $PbNi_{1.88}Mg_{0.12}V_2O_8$ splitting of the equally occupied, degenerate d_{z^2} and $d_{x^2-y^2}$ orbitals (zero-field splitting), may account for the tetragonal distortion of the NiO_6 octahedral units.

In a direct comparison of the raw data for the low-temperature (2 and 12 K) neutron diffraction profiles we observe no significant intensity difference between them, throughout the 2θ-range. In addition, all the Bragg peaks for the 2 K ($<T_N$) and 12 K ($>T_N$) high-resolution neutron data could be indexed by employing the same space group ($I4_1cd$) used at 300 K. That is to say no bulk structural phase transition accompanies the

---

[1] As the diffraction data were taken with diverse instrumental characteristics, dissimilar profile features, e.g. background treatment (polynomial fit or interpolation), peak-shape function, internal Si standard use, were recognized between the patterns. To this extent a different number of Rietveld refinable parameters was required for the optimum description of the diffraction profiles at different temperatures.
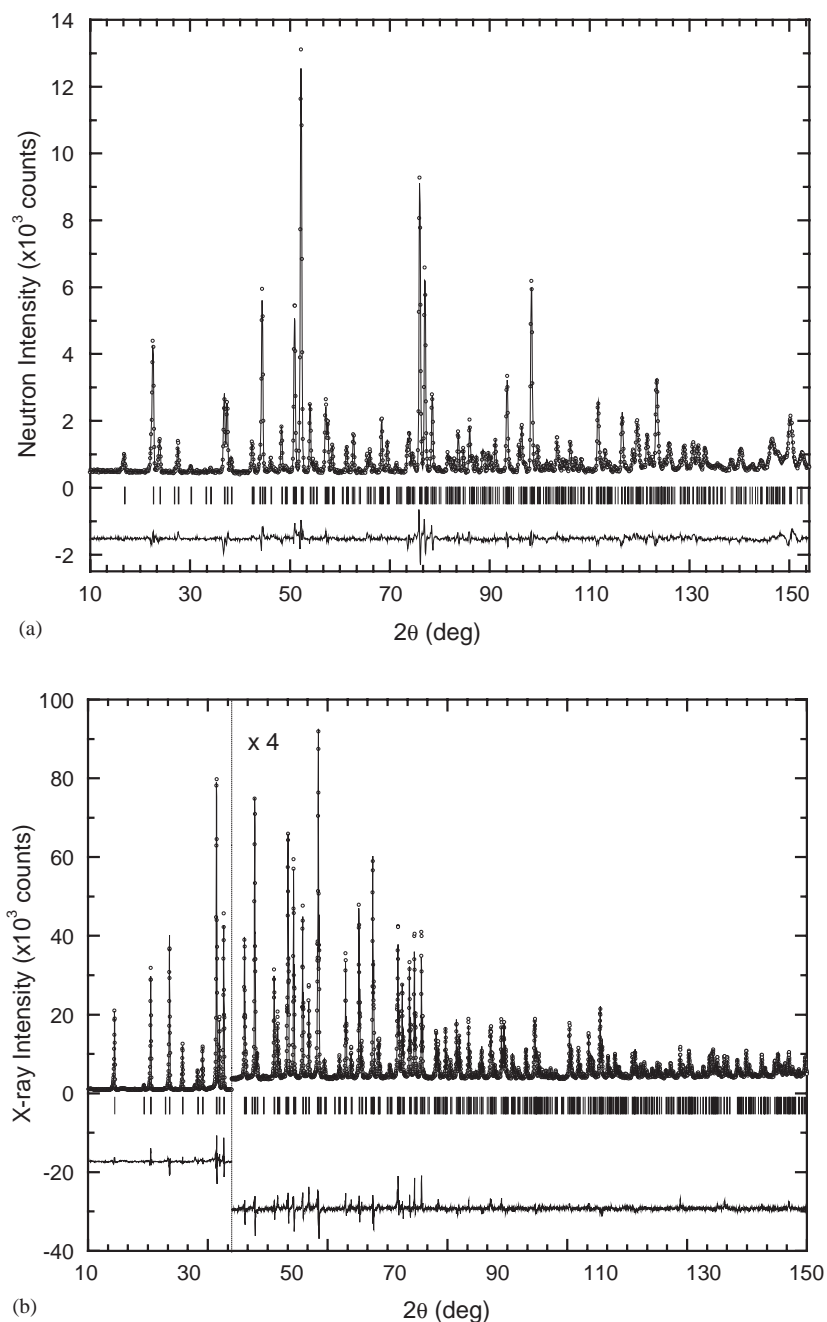
Fig. 4. Combined Rietveld refinement of the high-resolution neutron (a) and X-ray (b) powder diffraction patterns (open circles) for $PbNi_{1.88}Mg_{0.12}V_2O_8$ at 300 K. The solid line is the calculated profile and vertical marks indicate the position of the allowed Bragg reflections. The difference curves are plotted at the bottom of the figures.

magnetic ordering. Scattering at Bragg positions (Fig. 2) associated with the magnetic structure of $PbNi_{1.88}Mg_{0.12}V_2O_8$ is barely observable in the 2 K data, due to the lower neutron intensity at the E9 diffractometer, which would require extensively long counting statistics to resolve them. Atomic parameters for the V-atom at 2 K were taken from the Rietveld analysis of the combined XRD and NPD 12 K data. The refined fractional atomic coordinates and the isotropic Debye–Waller factors of the atoms in the unit cell at 2 K

are shown in Table 2c. Bond distances and selected angles are listed in Tables 3 and 4. It is worth noting that the anisotropic variation of the Ni–O bond lengths between 300 and 12 K results in a less pronounced elongation of the NiO_6 polyhedron at low temperatures. Non-isotropic variation in the remaining metal–oxygen bonds is also observed for the different cation environments.

The crystallographic parameters and bond distances obtained at 300 K by high-resolution NPD provide an

Table 1
Experimental conditions and refinement details of *combined* diffraction data for $PbNi_{1.88}Mg_{0.12}V_2O_8$ (numbers of N observations, P refined variables and C constraints are given)

Space group $I4_1cd$ ($Z = 8$)	$T = 300$ K		$T = 12$ K		$T = 2$ K	
	Neutron	X-ray	Neutron	X-ray	Neutron	
Cell parameters (Å)						
$a = b$		12.25008(4)		12.23211(11)		12.23134(7)
c		8.35891(4)		8.35014(9)		8.34991(5)
Volume (Å³)		1254.374(8)		1249.386(20)		1249.195(13)
2θ Range (deg)	10–154	10–130	10–154	13–120	10–155	10–155
Step size (deg)	0.0782	0.02	0.0781	0.02	0.0781	0.0782
Counting time (s/step)	—	29	—	50	—	—
Weighted profile R_{wp} (%)	6.61	8.26	5.81	12.5	5.82	5.34
Profile R_p (%)	5.09	6.07	4.38	9.57	4.48	4.08
Expected R_{exp} (%)	3.39	2.33	4.48	9.34	4.49	3.33
χ^2	3.81	12.50	1.69	1.78	1.68	2.57
Bragg R-factor (%)		6.36		4.19		4.48
Total no. of Independent Reflections	228	292	228	191	228	228
$N - P + C$	1814	5938	1807	4305	1812	1812
No. of refined parameters		38		45		43

Table 2

Atom	Wyckoff position	x/a	y/b	z/c	Occupancy	B_{iso} (Å²)
(a) Fractional coordinates and atomic thermal displacements from Rietveld refinement of *combined* neutron and X-ray powder diffraction data for $PbNi_{1.88}Mg_{0.12}V_2O_8$ at 300 K						
Pb	(8a)	0	0	0	0.5	0.67(2)
Ni	(16b)	0.3307(4)	0.3325(4)	0.1821(4)	0.931(9)	0.36(6)
Mg	(16b)	0.3307(4)	0.3325(4)	0.1821(4)	0.069(9)	0.36(6)
V	(16b)	0.2641(4)	0.0819(3)	0.0484(6)	1.0	0.26(8)
O(1)	(16b)	0.1472(6)	0.4945(14)	−0.0422(9)	1.0	0.62(6)
O(2)	(16b)	0.3352(11)	0.6741(11)	0.4365(8)	1.0	0.62(6)
O(3)	(16b)	0.1579(10)	0.6812(11)	0.6706(10)	1.0	0.62(6)
O(4)	(16b)	0.3252(7)	0.4990(15)	0.1610(9)	1.0	0.62(6)
(b) Fractional coordinates and atomic thermal displacements from Rietveld refinement of *combined* neutron and X-ray powder diffraction data for $PbNi_{1.88}Mg_{0.12}V_2O_8$ at 12 K						
Pb	(8a)	0	0	0	0.5	0.19(6)
Ni	(16b)	0.3287(2)	0.3322(3)	0.1764(6)	0.941(16)	0.24(5)
Mg	(16b)	0.3287(2)	0.3322(3)	0.1764(6)	0.059(16)	0.24(5)
V	(16b)	0.2587(13)	0.0817(11)	0.0428(25)	1.0	0.74(34)
O(1)	(16b)	0.1478(5)	0.4950(8)	−0.0532(9)	1.0	0.35(4)
O(2)	(16b)	0.3387(7)	0.6691(7)	0.4341(8)	1.0	0.35(4)
O(3)	(16b)	0.1607(8)	0.6834(5)	0.6700(10)	1.0	0.35(4)
O(4)	(16b)	0.3259(5)	0.4984(7)	0.1497(9)	1.0	0.35(4)
(c) Fractional coordinates and atomic thermal displacements from Rietveld refinement of two, *combined* data sets for the NPD data of $PbNi_{1.88}Mg_{0.12}V_2O_8$ at 2 K. Vanadium parameters are taken from the 12 K structure						
Pb	(8a)	0	0	0	0.5	0.16(4)
Ni	(16b)	0.3287(2)	0.3324(2)	0.1761(4)	0.930(11)	0.17(3)
Mg	(16b)	0.3287(2)	0.3324(2)	0.1761(4)	0.070(11)	0.17(3)
V	(16b)	0.2587	0.0817	0.0428	1.0	0.74
O(1)	(16b)	0.1480(3)	0.4947(5)	−0.0543(6)	1.0	0.27(3)
O(2)	(16b)	0.3388(4)	0.6693(4)	0.4338(5)	1.0	0.27(3)
O(3)	(16b)	0.1603(5)	0.6833(3)	0.6689(6)	1.0	0.27(3)
O(4)	(16b)	0.3254(3)	0.4987(4)	0.1488(6)	1.0	0.27(3)

empirical way to discuss the 'formal' valences of the different metal ions in $PbNi_{1.88}Mg_{0.12}V_2O_8$. The approach we follow here is the valence bond method as described by Brown and Altermatt [28]. It is a simple but powerful procedure for obtaining an insight into the cation oxidation state as inferred from its observed

Table 3
Selected bond lengths and bond valence sums (BVS) for PbNi$_{1.88}$Mg$_{0.12}$V$_2$O$_8$

	Bond (Å)	300 K	BVS	Deviation from ideal valence (%)	12 K	2 K
Pb	O(1)	2.505(13) × 2	1.914	4	2.443(9) × 2	2.440(5) × 2
		3.036(12) × 2			3.111(8) × 2	3.121(5) × 2
	O(2)	2.984(13) × 2			2.911(9) × 2	2.912(5) × 2
	O(3)	3.018(12) × 2			3.057(9) × 2	3.054(5) × 2
	O(4)	3.552(8) × 2			3.618(7) × 2	3.628(5) × 2
		2.529(8) × 2			2.470(7) × 2	2.471(4) × 2
Ni/Mg	O(1)$_E$	2.034(9)	2.082	4	2.055(7)	2.052(4)
	O(2)$_E$	2.055(8)			2.028(9)	2.027(6)
	O(2)$_A$	2.056(14)			2.091(9)	2.096(6)
	O(3)$_E$	2.003(9)			2.041(10)	2.035(7)
	O(3)$_A$	2.126(13)			2.064(11)	2.070(6)
	O(4)$_E$	2.048(18)			2.045(10)	2.047(6)
	⟨Ni–O⟩	2.054(12)			2.054(9)	2.055(6)
	⟨Ni–O$_E$⟩	2.035(12)			2.042(9)	2.040(6)
	⟨Ni–O$_A$⟩	2.091(14)			2.078(10)	2.083(6)
	$d_{Ni–Ni}$//	[100] [010]			[100] [010]	[100] [010]
	Ni–Ni^a of same z-coordinate	6.44 6.45			6.41 6.44	6.41 6.44
	Ni–Ni^a of $c/4$ Relative shift	6.45 6.45			6.42 6.42	6.42 6.42
V	O(1)	1.703(13)	4.985	~0	1.754(18)	1.757(18)
	O(2)	1.714(12)			1.767(20)	1.763(20)
	O(3)	1.743(12)			1.684(19)	1.687(19)
	O(4)	1.765(13)			1.705(19)	1.694(19)
	O(1)–V–O(2)	3.417(18)			3.521(27)	3.520(27)
	O(3)–V–O(4)	3.508(18)			3.389(27)	3.381(27)
	⟨V–O⟩	1.731(13)			1.728(19)	1.725(19)

^{a} Nickels located on adjacent chains. The distances, $d_{Ni–Ni}$, parallel to [1 0 0] and [0 1 0] directions are shown. The upper limit of the estimated standard deviation in the $d_{Ni–Ni}$ is ±0.01 Å.

Table 4
Selected bond angles in PbNi$_{1.88}$Mg$_{0.12}$V$_2$O$_8$

Bond angle (deg)	300 K	12 K	2 K
O(2)$_A$–Ni–O(3)$_E$	92.2(8)	90.7(6)	90.8(4)
O(2)$_E$–Ni–O(3)$_A$	88.8(7)	91.9(6)	91.8(4)
Ni–O(3)$_A$–Ni	88.9(5)	88.7(5)	88.8(3)
Ni–O(2)$_E$–Ni	89.4(5)	88.3(4)	88.3(3)
O(3)$_A$–V–O(4)$_E$	95.5(9)	98.1(5)	97.7(3)
O(1)$_E$–V–O(2)$_A$	91.3(7)	95.0(8)	95.0(3)

coordination to nearby anions and the associated bond lengths. The so-called bond valence sums (BVS) are calculated by the expression: $\mathrm{BVS} = \sum_i \exp[(r_0 - r_i)/B]$. Here, B is an empirically determined parameter of 0.37 Å, r_i is the experimentally determined bond length of the particular cation to the ith anion in its neighborhood and r_0 is the corresponding theoretically calculated bond distance. We employed the program VALIST [29], with internal tables for r_0. The results of the BVS calculations are listed in Table 3. The BVS value and the formal oxidation state for each atom are in reasonable agreement, as they deviate no more than 0.1 valence units (v.u.). The Ni/Mg BVS value has been averaged taking into account their occupation factors and their random distribution into the same crystallographic position. To this extent, the consistency of the results produces additional confidence regarding the accuracy of the experimentally determined bond-lengths that are used in the following discussion.

3.4. Lattice topology effects

In the PbNi$_{1.88}$Mg$_{0.12}$V$_2$O$_8$ compound the presence of impurities stabilizes the $S = 1/2$ end-of-chain spins [7,11,13] at either side of the randomly distributed Mg-ions ($S = 0$; spin vacancies). The enhancement of intra-chain coupling with decreasing temperature together with the inter-chain interaction of the vacancy-induced free spins could act in 'synergy' to stabilize a LRO ground state. According to our analysis, the nearest-neighbor (nn) Ni–Ni distance within the chains contracts from 2.892(6) Å (300 K) to 2.869(5) Å (12 K) when the temperature is reduced towards the T_N. Below T_N this nn distance remains unchanged within the accuracy of the experiment, i.e. 2.871(5) Å (2 K). Although the 300–12 K change is a relatively small one, namely −0.80 ±0.27%, it can be expected to affect the intra-chain
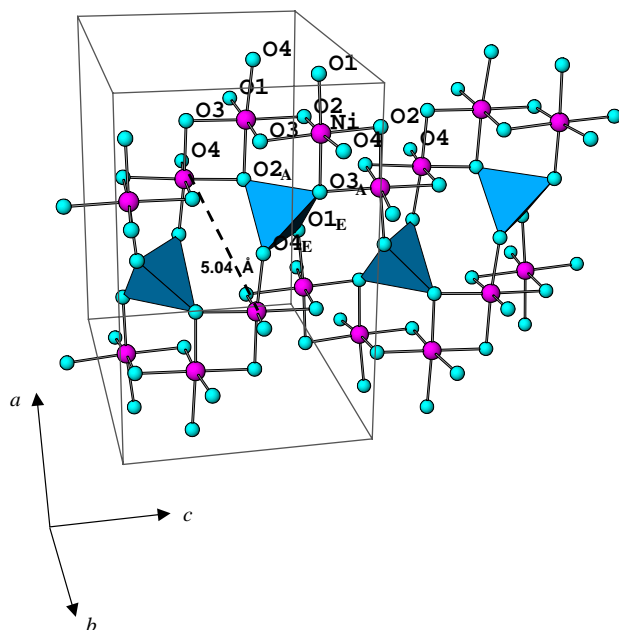
Fig. 5. Representation of the $PbNi_{1.88}Mg_{0.12}V_2O_8$ crystal structure showing the distorted arrangement of the 'twinned' spiral Ni chains. Note that the interaction pathway for two next-nearest-neighbor (*nnn*) Ni ions on adjacent chains passes through the VO_4 tetrahedra.

antiferromagnetic coupling, J, between *nn* Ni-spins. We note that, in simple terms, the magnitude of the superexchange interaction for overlapping $3d-2p$ orbitals depends strongly on the hopping integral, t_{pd}, namely, $J \sim t_{pd}^4$ [30]. In powder experiments such as the present one, it is difficult to estimate the absolute value of J; however, qualitatively we expect an increase in the hopping integral, as it depends strongly on the superexchange path-length, R, according to the relation $t_{pd} \sim 1/R^n$. Since the exponent, n, in insulating oxides is generally found to be a large number (i.e., $10 < n < 12$) [31], we anticipate that the *local geometry* plays a major role in determining the ground state magnetic properties of the $PbNi_{1.88}Mg_{0.12}V_2O_8$.

As such it is worth examining an extra factor, that is, the V^{5+} (d^0) atoms as mediators of the inter-chain interactions, J'. It has been mentioned before [8] that this vanadate system provides two pathways of coupling between Ni ions in different chains (Fig. 5). One of them couples two Ni^{2+} ions on adjacent chains with the same *c*-axis fractional coordinate. The other one couples two Ni^{2+} ions offset relative to each other by $c/4$ along the *c*-axis. Nevertheless, inelastic neutron scattering work [8] on the *parent* $PbNi_2V_2O_8$ material has pointed out that in such a polycrystalline quasi-one-dimensional solid it cannot be definitely determined which one of the above-mentioned next-nearest neighbor (*nnn*) inter-chain magnetic exchange pathways is the most favorable one. The static average magnetic structure, shown as an inset of Fig. 3, indicates that the *localized nnn* interaction for the Mg-*doped* compound produces an

'effective' antiferromagnetic coupling for the first type of pathway and a ferromagnetic one for the second. In order to get some clues we focus on the latter Ni–Ni interaction which takes place through $O(3)_A$–V–$O(4)_E$ or $O(1)_E$–V–$O(2)_A$ pathways (Fig. 5).

The observed V–O bonds between 300 and 12 K change anisotropically and suggest an apparent 'balancing' of the bonding interactions around the VO_4 tetrahedra. That is to say, within the standard errors of the refinements, the $O(1)_E$–V–$O(2)_A$ length expands as much as the $O(3)_A$–V–$O(4)_E$ pathway contracts. The refined values of relevant bond lengths are compiled in Table 3. Furthermore, between the 12 and 2 K structures there are no significant differences for any of the atomic positions in the unit cell, thus we assume that the position of V does not change as well. We can infer for its role below T_N through the 'shifts' of the surrounding metal–oxygen atomic positions. As the Ni–O and Pb–O distances between 12 and 2 K do not change significantly, when cooling through T_N, it is reasonable to assume that the size and shape of VO_4 tetrahedron is not changed below T_N. Then we can base our arguments on the modifications of the corresponding Ni–O distances along the magnetic exchange pathways [Ni–$O(1)_E$–V–$O(2)_A$–Ni or Ni–$O(3)_A$–V–$O(4)_E$–Ni], that effectively alter the *nnn* Ni–Ni separation.

An important observation here is that when the system is cooled from 300 to 2 K, the *shortest* Ni–Ni separation for atoms on the twinned chains remains unchanged, i.e. at $d_{Ni-Ni} = 5.04$ Å (magnetically coupled nickels by *direct* exchange) (Fig. 5). However, when we inspect how the *longer* Ni–Ni distances, $\langle d_{Ni-Ni} \rangle \sim 6.4$ Å, evolve upon cooling we find that there is a reduction ($\Delta d_{Ni-Ni}^{max} \cong -0.45\%$) in all the interchain *nnn* distances (magnetically coupled nickels by *superexchange* via VO_4 tetrahedra). The Ni–Ni lengths shown in Table 3 correspond to distances pairing Ni ions (on twinned chains running parallel to the *ac*-plane; Fig. 5) along the [100] direction and Ni ions (on consecutive twinned chains) along [010] direction. The estimated standard deviations for the *nnn* Ni distances, calculated from the errors on the refined atomic positions, are between $0.005 \leqslant \Delta d_{Ni-Ni} \leqslant 0.01$ Å. Such a small deviation on the *nnn* separations adds to the statistical accuracy of the quoted changes. When we examine the *nnn* distances connecting Ni ions with the same *z*-coordinate (Table 3), we note a comparable contraction.

We postulate that the subtle modification of the Ni separation on adjacent chains (*nnn*) indicates the proximity for the chains upon cooling. This in effect may bring on enhanced inter-chain coupling, J', for the $S = 1/2$ 'edge spins' around the Mg-impurities of this low-dimensional system. The findings are in agreement with recent ESR experiments [16], which have probed such a coupling and theoretical arguments [17], which

have suggested a possible microscopic mechanism. The highlighted changes in the topology of the nuclear structure establish an improved inter-chain coupling, which together with the enhancement of the intra-chain coupling, J, and reduction of thermal fluctuations at low-temperatures are essential for inducing LRAFO in $PbNi_{1.88}Mg_{0.12}V_2O_8$.

However, in another well-known Haldane gap system, the Y_2BaNiO_5, generating topological disorder by severing the Ni-chains when non-magnetic cations, such as Zn^{2+} or Mg^{2+}, are substituted at the Ni-sites does not support a transition to LRO [32–34]. This is despite the existence of $S = 1/2$ degrees of freedom created by breaking up the $S = 1$ spin-chains [35], similarly to the $PbNi_{1.88}Mg_{0.12}V_2O_8$ compound, which however illustrates the unusual effect of LRAFO induced by non-magnetic doping. Only in cases where Y^{3+} is replaced by a magnetic rare earth ion the system crosses over from the 1D disordered ground state to 3D magnetic order [24,36]. The model quasi-one-dimensional $Y_2Ba-NiO_5$ material [37], which shows Haldane gap behavior and strong intra-chain interactions along very short – Ni–O–Ni– bonds, in vertex sharing octahedra, does not promote LRAFO due to long pathways for inter-chain magnetic exchange.

4. Conclusions

We have studied the crystal structure and magnetic properties of the quasi-one-dimensional compound $PbNi_{1.88}Mg_{0.12}V_2O_8$ by employing Rietveld analysis of *combined* X-ray and neutron powder diffraction data as well as magnetic susceptibility measurements. The Haldane gap in the magnetic excitation spectrum of the undoped $PbNi_2V_2O_8$ compound is suppressed in the Mg-substituted ($x \cong 0.12$) system and a long-range antiferromagnetic ordering takes place below $T_{Néel} \cong 3.4$ K. The critical behavior of the sublattice magnetization [exponent $\beta = 0.31(3)$] postulates the existence of an *Ising*-like, easy-axis anisotropy for the resolved spin-configuration. Also the reduced magnitude of the staggered moment [$0.98(3) \mu_B/Ni^{2+}$] points to the importance of 'zero-point' spin fluctuations in this system. The Rietveld analysis of the powder diffraction data indicates that the magnetic transition at $T_N \cong 3.4$ K is not accompanied by a structural phase transformation. The *subtle lattice topology* plays a major role in determining the ground state magnetic properties. We have investigated the modification of the bond distances upon cooling and their role in stabilizing the long-range ordered state. The pathway involving the VO_4 tetrahedra mediates the magnetic exchange interaction between adjacent chains (inter-chain coupling, J'). We suggest that the magnetic coupling of the free $S = 1/2$ spins at the end of Ni chains is assisted by the modification of Ni–Ni distances. The latter indicates that the NiO_6 chains show a tendency to approach each other at low temperatures. These factors together with the enhancement of the intra-chain Ni–Ni correlations most likely drive the system to Néel ordering.

References

[1] J.W. Bray, H.R. Hart Jr., L.V. Interrante, I.S. Jacobs, J.S. Kasper, G.D. Watkins, S.H. Wee, J.C. Bonner, Phys. Rev. Lett. 35 (1975) 744.

[2] F.D.M. Haldane, Phys. Rev. Lett. 50 (1983) 1153.

[3] J.G. Bednorz, K.A. Müller, Z. Phys. B 64 (1986) 189.

[4] M. Hase, I. Terasaki, K. Uchinokura, Phys. Rev. Lett. 70 (1993) 3651.

[5] M. Hase, I. Terasaki, Y. Sasago, K. Uchinokura, H. Obara, Phys. Rev. Lett. 71 (1993) 4059.

[6] S.B. Oseroff, S.-W. Cheong, B. Aktas, M.F. Hundley, Z. Fisk, L.W. Rupp Jr., Phys. Rev. Lett. 74 (1995) 1450.

[7] Y. Uchiyama, Y. Sasago, I. Tsukada, K. Uchinokura, A. Zheludev, T. Hayashi, N. Miura, P. Böni, Phys. Rev. Lett. 83 (1999) 632.

[8] A. Zheludev, T. Masuda, I. Tsukada, Y. Uchiyama, K. Uchinokura, P. Böni, S.H. Lee, Phys. Rev. B 62 (2000) 8921.

[9] R. Wichmann, H.K. Müller-Buschbaum, Rev. Chim. Miner. 23 (1986) 1.

[10] A. Lappas, V. Alexandrakis, J. Giapintzakis, V. Pomjakushin, K. Prassides, A. Schenck, Phys. Rev. B 66 (2002) 14428.

[11] E.F. Shender, S.A. Kivelson, Phys. Rev. Lett. 66 (1991) 2384.

[12] K. Uchinokura, Y. Uchiyama, T. Masuda, Y. Sasago, I. Tsukada, A. Zheludev, T. Hayashi, N. Miura, P. Böni, Physica B 284 (2000) 1641.

[13] E.S. Sorensen, I. Affleck, Phys. Rev. B 49 (1994) 15771.

[14] I. Affleck, T. Kennedy, E.H. Lieb, H. Tasaki, Phys. Rev. Lett. 59 (1987) 899.

[15] A.I. Smirnov, V.N. Glaskov, H.-A. Krug von Nida, A. Loidl, L.N. Demianets, A.Ya. Shapiro, Phys. Rev. B 65 (2002) 174422.

[16] A. Zorko, D. Arčon, A. Lappas, J. Giapintzakis, C. Saylor, L.C. Brunel, Phys. Rev. B 65 (2002) 144449.

[17] A. Zheludev, T. Masuda, K. Uchinokura, S.E. Nagler, Phys. Rev. B 64 (2001) 134415.

[18] J. Rodríguez-Carvajal, Physica B 192 (1993) 55.

[19] I. Mastoraki, A. Lappas, R. Schneider, J. Giapintzakis, Appl. Phys. A 74 (Suppl.) (2002) S640.

[20] G. Shirane, Acta Crystallogr. 12 (1959) 282.

[21] P.E. Cox, V.J. Minkiewicz, Phys. Rev. B 4 (1971) 2209.

[22] R. Sáez-Puche, J. Hernández-Velasco, Adv. Mater. Res. 1–2 (1994) 65.

[23] J. Hernández-Velasco, R. Sáez-Puche, J. Rodríguez-Carvajal, Physica B 234–236 (1997) 569.

[24] E. García-Matres, J.L. Martínez, J. Rodríguez-Carvajal, Eur. Phys. J. B 24 (2001) 59.

[25] F.C. Malcolm, Magnetic Critical Scattering, Oxford University Press, New York, 1989.

[26] J.L. García-Muñoz, J. Rodríguez-Carvajal, P. Lacorre, J.B. Torrance, Phys. Rev. B 46 (1992) 4414.

[27] J.D. Jorgensen, B. Dabrowski, D.R. Shiyou Pei, D.G. Richards, Hinks, Phys. Rev. B 40 (1989) 2187.

[28] I.D. Brown, D. Altermatt, Acta. Crystallogr. B 41 (1985) 244.

[29] A.S. Wills, I.D. Brown, VALIST, CEA, France, 1999.

[30] W.A. Harrison, Electronic Structure and Properties of Solids, Freeman, San Francisco, 1980.

[31] H. Eskes, J.H. Jefferson, Phys. Rev. B 48 (1993) 9788; P. Millet, C. Satto, J. Bonvoisin, B. Normand, K. Penc, M. Albrecht, F. Mila, Phys. Rev. B 57 (1998) 5005.

[32] R. Sáez-Puche, J.M. Coronado, L.C. Otero-Díaz, J.M. Martín-Llorente, J. Solid State Chem. 93 (1991) 461.

[33] B. Batlogg, S.-W. Cheong, L.W. Rupp Jr., Physica B 194–196 (1994) 173.

[34] F.J. Mompeán, M. García-Hernández, J.L. Martínez, E. García-Matres, C. Prieto, A. de Andrés, R. Sáez-Puche, R.S. Eccleston, H. Schober, Physica B 234–236 (1997) 572.

[35] S. Kimura, H. Ohta, M. Motokawa, T. Yokoo, J. Akimitsu, J. Phys. Soc. Japan 67 (1998) 2514.

[36] A. Zheludev, Neutron News 10 (3) (1999) 16.

[37] J. Darriet, L.P. Regnault, Solid State Commun. 86 (1993) 409.